

# Experimental study on seismic behavior of frame structures composed of concrete encased columns with L-shaped steel section and steel beams

Lei Zeng\*, Wenting Ren, Zhengtao Zou, Yiguang Chen, Wei Xie and Xianjie Li

School of Urban Construction, Yangtze University, Jingzhou, Hubei, China

(Received November 9, 2017, Revised December 1, 2018, Accepted December 17, 2018)

**Abstract.** The frame structures investigated in this paper is composed of Concrete encased columns with L-shaped steel section and steel beams. The seismic behavior of this structural system is studied through experimental and numerical studies. A 2-bay, 3-story and 1/3 scaled frame specimen is tested under constant axial loading and cyclic lateral loading applied on the column top. The load-displacement hysteretic loops, ductility, energy dissipation, stiffness and strength degradation are investigated. A typical failure mode is observed in the test, and the experimental results show that this type of framed structure exhibit a high strength with good ductility and energy dissipation capacity. Furthermore, finite element analysis software Perform-3D was conducted to simulate the behavior of the frame. The calculating results agreed with the test ones well. Further analysis is conducted to investigate the effects of parameters including concrete strength, column axial compressive force and steel ratio on the seismic performance indexes, such as the elastic stiffness, the maximum strength, the ductility coefficient, the strength and stiffness degradation, and the equivalent viscous damping ratio. It can be concluded that with the axial compression ratio increasing, the load carrying capacity and ductility decreased. The load carrying capacity and ductility increased when increasing the steel ratio. Increasing the concrete grade can improve the ultimate bearing capacity of the structure, but the ductility of structure decreases slightly.

**Keywords:** frame structure; concrete encased column; L-shaped steel section; seismic behavior

## 1. Introduction

Over the last several decades, steel-concrete composite systems have been widely utilized in building structures and bridges, even in regions with high seismic risk, due to the ideal combination of the advantages of both steel and concrete. The concrete encased column is a typical steel-concrete composite member, in which steel skeleton are embedded in a reinforced concrete to improve the shear resistance of the column. The concrete encasement effective improves the resistance of the steel core against both local and over buckling. The concrete encasement also provides protection against corrosion from chemical and insulation from rapid temperature rise in the presence of fire. The concrete-encased columns have already been used in China, US and Japan (Deierlein and Noguchi 2004, Shanmugam and Lakshmi 2001). Therefore, the performance of concrete encased composite systems has caught more and more research attentions.

Based on the literature, a new form of concrete encased columns with irregular sections was proposed in frame structural system. T-, L-, cross-shaped steel were arranged in the column section to meet the architecture requirement (Xue *et al.* 2016, Xiao *et al.* 2017). The width of the columns is equal to the width of infilled walls, which makes a better use of available space and improves the aesthetic

appearance of structure. In practical engineering, the concrete encased steel frame with irregular sections mainly includes two basic types: (1) the middle frame with T-shaped for side columns (cross shaped for middle columns); (2) the exterior frame with L-shaped for corner columns (T-shaped for middle columns). Up to now, extensive studies on the concrete encased members with symmetrical steel section including members, joints and structural system have been carried out. Some investigations involving bond-slip between concrete and steel (Roeder *et al.* 1999, Zeng *et al.* 2015), the behavior of concrete encased beams (Tong *et al.* 2016, Piloto *et al.* 2017, Zhou *et al.* 2010), columns (Chen *et al.* 2018, Qi *et al.* 2011, Wang *et al.* 2015, Tokgoz and Dundar 2008, Pecce and Rossi 2013, Liu *et al.* 2014), beam-column joints (Lima *et al.* 2017, Liao *et al.* 2014), and frames (Fu *et al.* 2015, Zhang and Jia 2016, Zeng *et al.* 2017) have been reported. The above researches indicates that concrete-encased composite structure possess a smaller sectional dimension, higher load-carrying capacity, better fire resistance to fire and more excellent seismic behavior compared with reinforced concrete structures. The design calculation theory and construction method were given in building codes such as ACI 318-05 code, JGJ138-2001 specification, AIJ-SRC standard, EUROCODE 4 and AISC Manual of Steel Construction (American Concrete Institute 2004, China Academy of Building Research 2001, Architectural institute of Japan 2010, European committee for standardization 1994, American Institute of Steel Construction 2005).

Although the behavior of concrete encased steel composite columns has been extensively studied, many of

---

\*Corresponding author, Professor  
E-mail: [zenglei@yangtzeu.edu.cn](mailto:zenglei@yangtzeu.edu.cn)

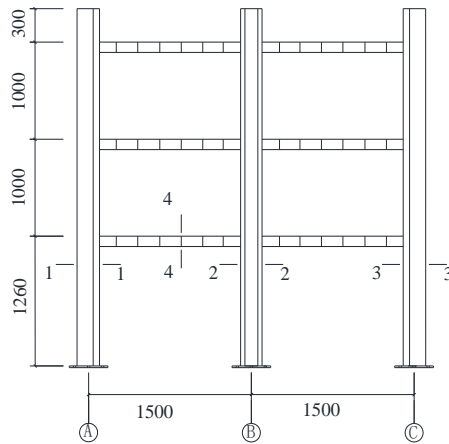


Fig. 1 Elevation of the specimen

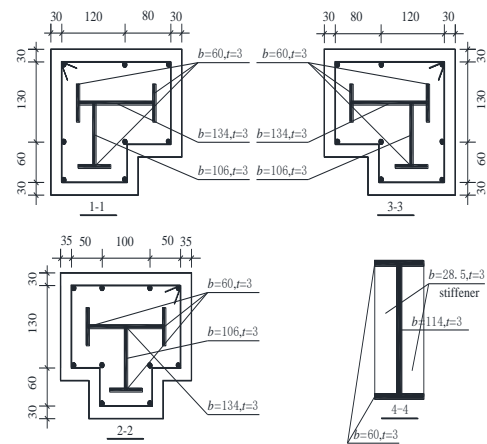


Fig. 2 The details of section and steel skeleton

the research works emphasized the composite columns with H-shaped structural steel section. However, very few methods and experimental researches were available for concrete-encased composite columns with unsymmetrical steel section such as T-shaped or L-shaped. Existing achievements mainly focused on calculation method of bending strength. Chen *et al.* (2006) developed an analytical model for predicting the force-deformation response for composite stub columns with various structural steel sections. Roik *et al.* (1990) has proposed a simplified approach for bending strength of concrete-encased composite columns with unsymmetrical steel by modifying the calculation method of bidirectional symmetrical steel given in the EUROCODE 4. Detailed experimental work for the seismic behavior of the concrete-encased composite members and structures are rather limited. There is also lack of concern for the design specifications on the concrete-encased members for the concrete-encased members with unsymmetrical steel sections.

Meanwhile, concrete-encased columns with unsymmetrical cross-sectional shapes, such as T-shape or L-shape, have been used in several high-rise frame structures in China. In this study, a frame structural system composed of Concrete encased columns with L-shaped steel section and steel beams is investigated. The seismic behavior of a 2-bay, 3-story and 1/3 scaled frame specimen is studied through combined experimental and numerical studies. The failure modes, damage process, load versus displacement relations, strain and displacement developments of typical specimens are displayed. Based on the test results, the effect of parameters on various indexes, such as the elastic stiffness, the maximum strength, the ductility coefficient, the strength and stiffness degradation, and the equivalent viscous damping ratio, are discussed.

## 2. Experimental program

### 2.1 Specimen design

An experimental study on the specimen was performed to assess the response of concrete encased steel frames under axial compression and cyclic horizontal load. The

experimental specimen was a 1/3 scale frame. The specimen has three stories and two spans. It was designed according to Chinese codes for GB50011-2010 (China Academy of Building Research 2010), GB50010-2010 (China Academy of Building Research 2010) and JGJ138-2001.

An experimental study on the specimen was performed to assess the response of concrete encased steel frames under axial compression and cyclic horizontal load. A typical multistory concrete-encased frame structure was used as the reference for extracting the experimental specimens. The bottom level, the intermediate level, and the top level were selected as the first-, the second- and the third- story of the prototype respectively for the analysis. The design of the structure and the element sections used were identical to a two-span, and three-story structure. The test specimen was 1/3 scaled. The spans measured 1.5m each. The storey heights are 1.26 m and 1m for the first story and the others, respectively. The structure was designed using the Chinese codes while keeping the effects of gravity loads (permanent and variable actions) and lateral loads (wind and seismic actions) in mind. The dead and live loads were both  $4.0 \text{ kN/m}^2$  and the reference wind pressure was  $0.35 \text{ kN/m}^2$ . The building site was characterized by a design ground acceleration of 0.2 g and a characteristic period of 0.4s. It should be noted that the seismic intensity and response spectrum used during the design were those given in the Chinese seismic code.

The specimen was consisted of concrete encased steel columns and steel beams. The encased structural steels were L- and T-shaped hot-rolled structural steel for edge and centre columns, respectively. The steel skeletons were welded with 3 mm thick steel plates. The longitudinal bars and stirrups are 8 mm and 4 mm in diameter, respectively. The spacing of stirrups is 50 mm at the ends of columns, but 100 mm in the other region. The concrete with 300 mm in height is reserved at the top of columns for installing the loading device. In order to simulate the boundary conditions in practical engineering, a steel plate with 20 mm in thick was welded at the column bottom, which is fixed by 10.9 grade M30 high strength shear bolt. The elevation of the specimen and details of section dimensions are shown in Figs. 1-2.

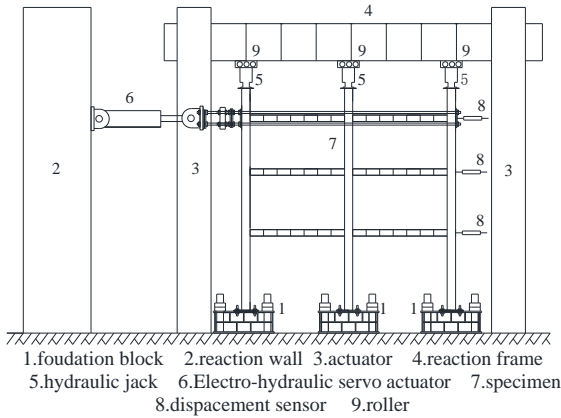


Fig. 3 Test setup



Fig. 4 Loading equipment and specimen

Table 1 Mix proportion of concrete

Concrete strength grade	Water (kg/m <sup>3</sup> )	Cement (kg/m <sup>3</sup> )	Sand (kg/m <sup>3</sup> )	Stone (kg/m <sup>3</sup> )
C30	243	494	914	1490

## 2.2 Material properties

The concrete was poured in a similar manner as in actual construction projects and was cured at an ambient temperature for 28 days. The C30 concrete is designed and fabricated according to laboratory mix proportion and used for the test specimen as shown in Table 1. The average compressive strength of nine 150 mm concrete cubes was measured as 35.02 MPa at 28 days. The stirrups and longitudinal bars are made of cold drawn steel at grade of HRB335, the elastic modulus  $E_s=2.1 \times 10^5$  MPa. The steel skeleton used in columns and beams is at grade of Q235 the elastic modulus  $E_{ss}=2.0 \times 10^5$  MPa. The material properties of steel are shown in Table 2.

## 2.3. Test setup and loading procedure

The quasi-static cyclic test was carried out by the electro-hydraulic servo system in the civil engineering laboratory of Yangtze University. The test setup and instrumentation are illustrated in Figs. 3-4. The constant axial compression was applied by vertical actuator on each column, while the reverse cyclic loading was applied by horizontal actuator. The axial compression simulated the column load caused by gravity and imposed load in practical engineering. Before the test, a pre-loading procedure was conducted. Due to the high design axial pressure value, a 500 kN axial load was loaded axially at the top of columns within 2 minutes. Then the axial load increased with an increment of 100 kN until reaching design value and keeping constant. The axial compression ratio was defined as Eq. (1)

$$n = N / (f_c A_c + f_y A_s + f_{ss} A_{ss}) \quad (1)$$

Where,  $n$  is the axial compression ratio and the value is 0.65,  $N$  is the actual axial pressure on the column in the test,  $f_c$  is the design value of axial compressive strength of concrete,  $A_c$  is the area of the concrete part in the column,  $f_y$

Table 2 Material properties of steel

Type	Diameter/ thickness (mm)	Yield strength (MPa)	Tensile strength (MPa)
Steel bar	Bb4	435	513
	B8	304	409
Q235 steel plate	3	327	481
	20	317	464

Table 3 Loading history

Loading history	Displacement (mm)	Cycles
1st	4	1
2nd	8	1
3rd	12	1
4th	16	3
5th	32	3
6th	48	3
7th	64	3
8th	80	3

is the design value of compressive strength of longitudinal reinforcement,  $f_{ss}$  is the value of compressive strength of section steel,  $A_{ss}$  is the area of section steel.

Displacement controlling method was adopted for horizontal loading and the loading history is shown in Table 3. The first three displacement level was applied by only one cycle, the following steps were repeated for three cycles with an increment of 4 mm per step. The experiment was finished until the loading dropped below 85% of the peak loading or the specimen was completely failure. Displacement transducers are installed at each layer to record the lateral displacement during the experiment. Strain gages were attached at the region of beams and columns end to measure the strain history. The arrangement of strain gauges is shown in Fig. 5.

## 3. Test results and analysis

### 3.1 Test phenomenon

At the beginning of loading, the specimen was in elastic

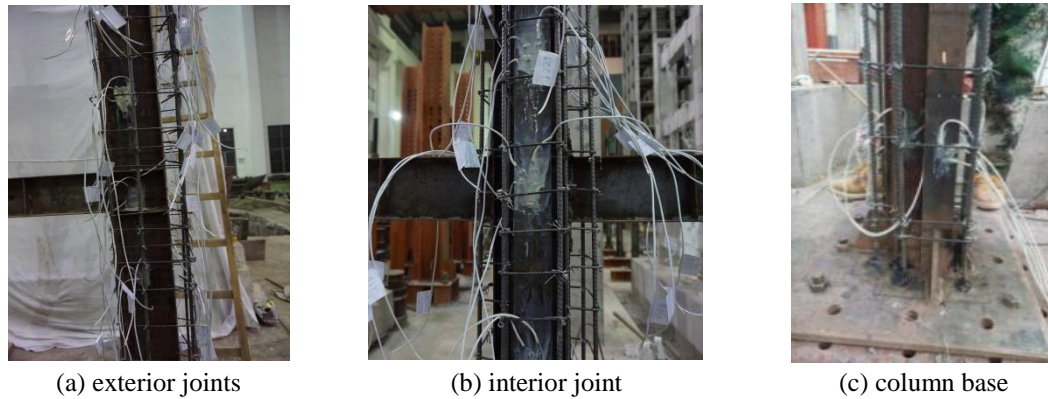


Fig. 5 Arrangement of strain gauges



Fig. 6 Failure of beam-end



Fig. 7 Concrete cracks at column base



Fig. 8 Failure of joints

stage. There was no obvious damage in the frame beams and columns, and the residual deformation was small after unloading. When the loading displacement reached 16mm, slight concrete cracks occurred at the beam-column joints and bottom of columns. With the increase of displacement, the buckling appeared at the flanges of beam-end in middle layer. The shear cracks were observed in the core area of joint and extended slowly as shown in Fig. 6. When the loading displacement reached 64 mm, the strain in the plastic hinge region of the beam-ends increased rapidly. The web plates at the beam-end bulged out, which meant that the plastic hinges appeared. As shown in Figs.7-8, the cracks at the bottom of column and core area of joints gradually extended. When the loading displacement reached 96 mm, several horizontal cracks formed at the exterior columns. The width and depth of oblique cracks in the joints developed and intersected as X-shape. When the loading displacement reached 112 mm, serious crushing and spalling of concrete in the joints occurred, the

reinforcements and steel skeleton were exposed. The specimen was failure as the bearing capacity decreased to 85% of the ultimate load, and the experiment was finished.

Under the action of low cyclic loading, the specimen is characterized by beam hinge failure mechanism. Fig. 9 shows the plastic hinge mechanism, the plastic hinges primarily occur in the second layer, which points out the weak region. The specimen exhibits classical failure of beam hinge. Fig. 10 shows the measured strain of steel skeleton. The directions for horizontal, vertical and oblique are pointed out,  $\Delta$  is the horizontal displacement at the third layer. The strain at the base and second layer reaches nearly  $3000\mu\epsilon$ , which is larger than other components. It can be seen that the specimen generally meet requirements of “strong column-weak beam, strong shear-weak bending and strong joints-weak member” in design codes.

### 3.2 Hysteretic curve

The hysteretic curve reflects the relation between the stress and deformation of the structure, and it is the basis of nonlinear seismic response analysis. As shown in Fig. 11,

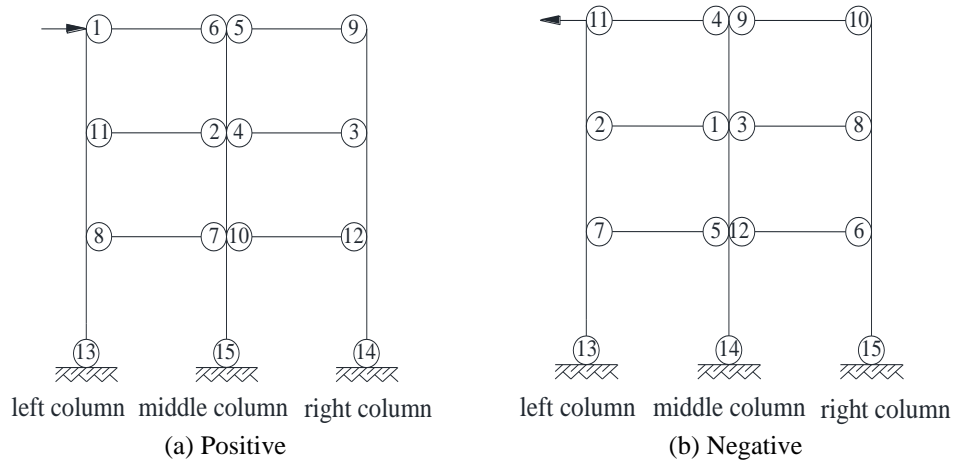


Fig. 9 Subsequence of plastic hinges

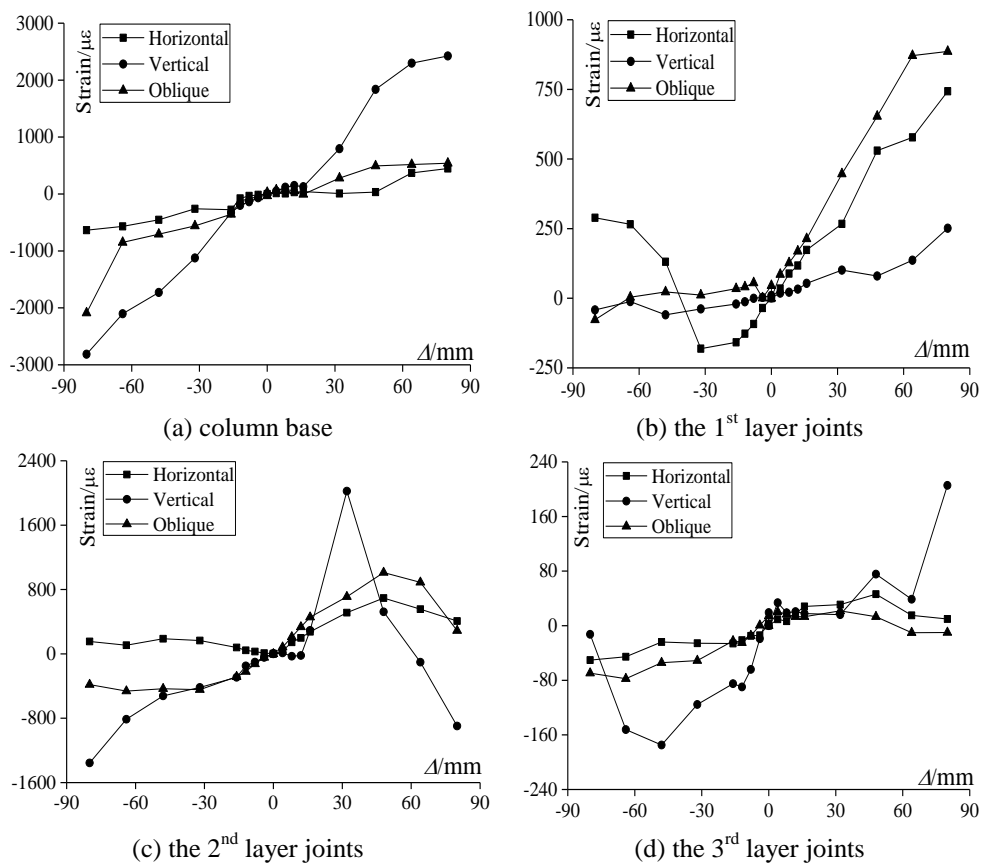


Fig. 10 Measured strain

where  $P$  is the horizontal load corresponding to the horizontal displacement  $\Delta$ . The results indicate that the specimen experiences elastic, plastic and failure stage under the action of low cyclic loading. Firstly the frame is in elastic stage, and the hysteretic curve is linear and the loading path coincides with unloading one. With horizontal displacement increased, micro-cracks appeared in the joints and column base. The curve gradually deviated from the straight line, and the residual deformation enlarged. The area of the hysteresis loop and peak load at each displacement level increased, the specimen entered into the elastic-plastic stage. The peak load at latter two cycles of

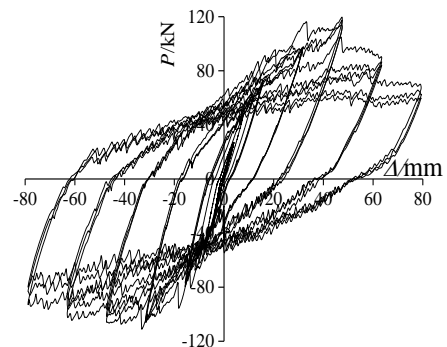


Fig. 11 Hysteretic curve

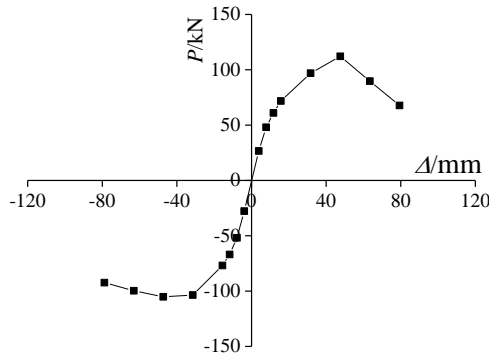


Fig. 12 Skeleton curve

Table 4 The load and displacement at each stage

$P_y$ /kN		$\Delta_y$ /mm		$P_{max}$ /kN		$\Delta_{max}$ /mm		$P_u$ /kN		$\Delta_u$ /mm	
+	-	+	-	+	-	+	-	+	-	+	-
80.41	78.69	21.22	20.68	112.17	105.17	47.59	45.29	95.34	92.32	63.54	72.85

one displacement level decreased gradually, which showed the damage of specimen. Finally, the hysteresis loop seriously inclined to the horizontal axis with the rapid decline of bearing capacity. In general, the shape of hysteretic curve is plump and in shuttle-shaped, Pinching effects are not obviously observed. The specimen performs good hysteretic behavior and higher energy dissipation capacity.

### 3.3 Skeleton curve

Fig. 12 shows the skeleton curve, it is approximately parabolic with obvious ascending and descending segments. The skeleton curve decreases slowly after reaching the peak load, specimen shows good ductility after yielding. The equivalent energy method is adopted to determine the yield point. The load and displacement of the specimen at different stages are shown in Table 4, where  $P_y$  and  $\Delta_y$  stand for the yielding load and displacement of the frame,  $P_{max}$  and  $\Delta_{max}$  stand for the ultimate load and displacement, and  $P_u$  and  $\Delta_u$  stand for the failure load and failure displacement respectively.

### 3.4 Ductility and energy dissipation capacity

The displacement ductility coefficient ( $\mu = \Delta_u / \Delta_y$ ) and inter-story drift ( $\theta = \Delta / \Delta H$ ) are key indexes to judge the structural deformation capacity, where  $\Delta_u$  and  $\Delta_y$  are the story drift corresponding to Table 4,  $\Delta$  is the story drift at yielding, ultimate or failure load, and  $\Delta H$  is the floor height. According to Chinese Code for Seismic Test Method of Buildings (JGJ101-96) (China Academy of Building Research 1997), the equivalent damping coefficient ( $h_e$ ) is used to determine the energy dissipation capacity of specimen. The equivalent damping coefficient ( $h_e$ ) and energy dissipation coefficient ( $E$ ) can be defined as Eqs. (2)-(3)

$$h_e = \frac{1}{2\pi} \cdot E \quad (2)$$

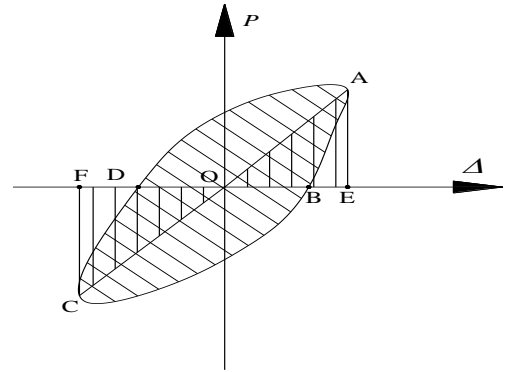


Fig. 13 Calculation of energy dissipation coefficient

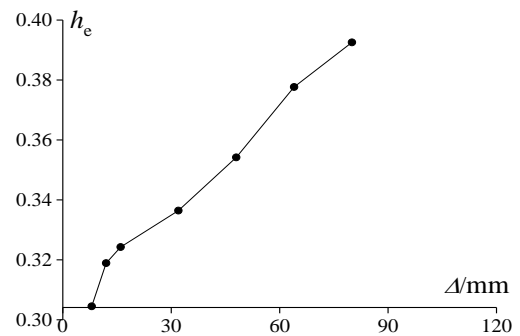


Fig. 14 Equivalent viscous damping coefficient

$$E = \frac{S_{ABCD}}{S_{OAE} + S_{OCF}} \quad (3)$$

where  $S_{ABCD}$  is the area under curves ABCD as shown in Fig. 13,  $S_{OAE}$  and  $S_{OCF}$  are the areas within the triangles OAE and OCF.

Table 5 lists the calculated ductility coefficient and the story drift. It can be seen that the ductility coefficients are nearly 3 and the maximum story drift are 1/45, which meets the requirements of the specification GB50011-2010. The specimen has better deformation ability under earthquake action. Fig. 14 shows the relationship between equivalent viscous damping coefficient and loading displacement.  $h_e$  is larger than 0.3 during the loading process and the maximum value reaches 0.4 at failure stage. When horizontal displacement exceeds 32mm, plastic rotation at beam-ends gradually occurs which resulting to the plastic hinge. At the same time, the concrete crushed and the steel of the column base yielded. The energy is absorbed by this deformation behavior, it indicates that the material performance is fully utilized in frame structure with L-shaped concrete encased columns and steel beams.

### 3.5 Strength and stiffness degradation

The strength degradation coefficient ( $\lambda_i = P_i / P_{max}$ ) is used to analyze the strength degradation law of the specimen during the whole test, where  $P_i$  is the peak load at  $i$ -th cycles and  $P_{max}$  is the ultimate load. Through the secant stiffness ( $K_i = \pm |P_i| / |\Delta_i|$ ), the degradation of the lateral stiffness of the specimen can be obtained, where  $\Delta_i$  is the displacement corresponding to  $P_i$ . Fig. 15 shows the

Table 5 Ductility coefficient and story drift

Layer	$\mu$		Yielding stage ( $\theta_y$ /rad)		Ultimate stage ( $\theta_{max}$ /rad)		Failure stage ( $\theta_u$ /rad)	
	+	-	+	-	+	-	+	-
3	2.98	4.91	1/143	1/158	1/64	1/62	1/48	1/32
2	3.19	2.51	1/139	1/121	1/62	1/68	1/44	1/48
1	2.81	2.83	1/179	1/169	1/80	1/86	1/64	1/60
Average	3.00	3.52	1/154	1/158	1/69	1/72	1/51	1/45

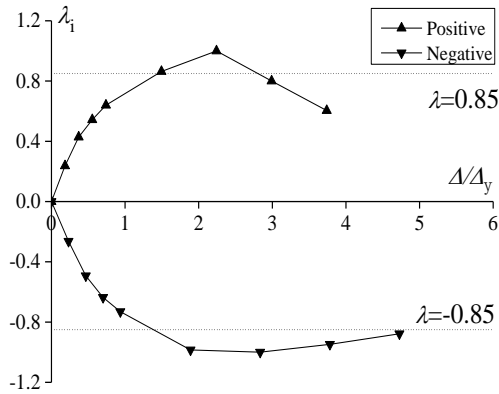


Fig. 15 Strength degradation curves

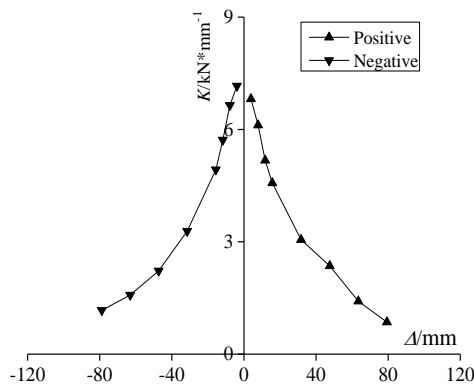


Fig. 16 Secant stiffness curves

relationship between the strength degradation coefficient  $\lambda_i$  and  $\Delta/\Delta_y$ . It indicates that with the increase of the displacement, the strength degradation coefficients in two loading directions primarily increase and then decrease. The strength degradation curves of the specimen has an obvious ascending segment after yielding, it indicates that the specimen owns a certain safety reserve. Fig. 16 shows the relationship between secant stiffness with loading displacement, the tendency in the positive and negative direction is similar. At initial stage the stiffness degradation rate is equal. As the concrete cracks at column and joints develop, the stiffness rapidly degenerates. Then the plastic hinge appears which plays the role of dissipating energy. At failure stage the rate of stiffness degradation slow down, the specimen performs good seismic performance.

### 3.6 Deformation recovery capability

The deformation recovery capacity of structure is an important index to determine the seismic performance. Fig.

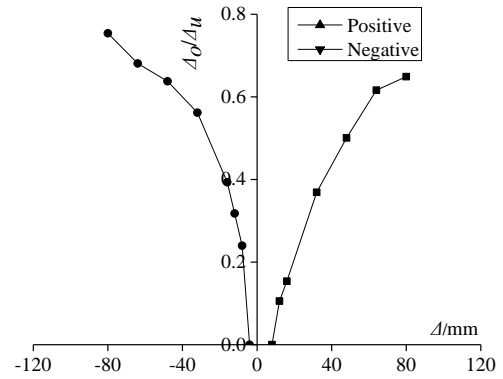


Fig. 17 Ratio of residual deformation

17 shows the residual deformation rate ( $\Delta_o/\Delta$ ), where  $\Delta_o$  is the residual deformation in the first cycle at each level. At initial stage the specimen is elastic and the residual deformation is relative small. With the increment of loading displacement, the frame enters into yield stage and the residual deformation increases gradually. At failure stage residual deformation rate is about 0.8. In a word, the specimen possesses good resistance to plastic deformation.

## 4. Finite element analysis

The Perform-3D is used for three-dimensional nonlinear finite element analysis on the frame to study the seismic behavior of structures. It has advantages in rich element types, efficient nonlinear analysis algorithm and perfect structure performance evaluation system. At present, it has been widely used in the analysis for structural seismic performance.

### 4.1 Material and element model

Perform-3D provides three kinds of nonlinear constitutive models, including non buckling type, tensile type only and buckling type. In this paper, steels are made of non buckling reinforced material and the skeleton curve is in the form of three-fold lines, as shown in Fig. 18. The skeleton curve of steel includes three segments: OY and YU are the elastic and hardening stages, "X" is the failure point. The concrete materials can be divided into confined concrete and unconfined concrete. The skeleton curve for concrete constitutive model is in the form of five-fold lines based on Mander model as shown in Eqs (4)-(9) (Mander *et al.* 1988), and the compressive stress-strain curve of concrete provided in the Chinese Code for Design of Concrete Structures (GB50010-2010). In Fig. 19 the concrete skeleton curve contains 5 key points ("Y", "U", "L", "R" and "X"), where the meaning of OY, YU and "X" are consistent with the above, "L" and "R" represent the end of plastic stage and beginning of residual bearing capacity. UL and LR stand for the plastic platform section and the significant degradation.

$$f_c = \frac{f'_{cc} x r}{r - 1 + x^r} \quad (4)$$

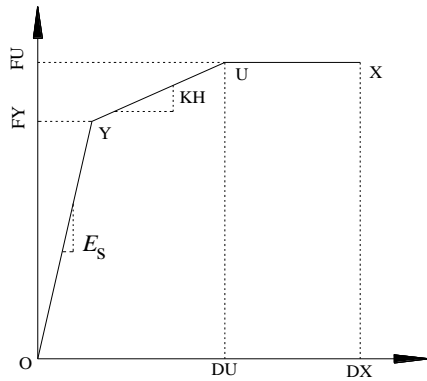


Fig. 18 Skeleton curve of steel

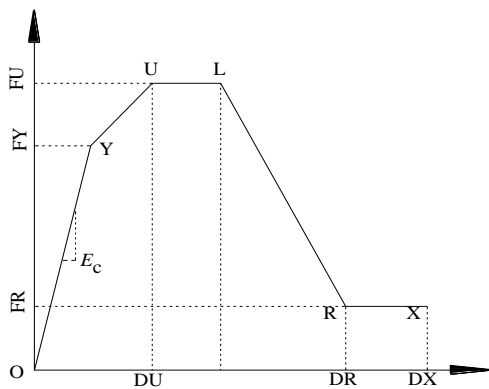


Fig. 19 Skeleton curve of concrete

$$x = \frac{\varepsilon_c}{\varepsilon_{cc}} \quad (5)$$

$$\varepsilon_{cc} = \varepsilon_{co} \left[ 1 + 5 \left( \frac{f'_{cc}}{f'_{co}} - 1 \right) \right] \quad (6)$$

$$r = \frac{E_c}{E_c - E_{sec}} \quad (7)$$

$$E_c = 5000 \sqrt{f'_{co}} \quad (8)$$

$$E_{sec} = \frac{f'_{cc}}{\varepsilon_{cc}} \quad (9)$$

Where  $f_c$  and  $\varepsilon_c$  is compressive stress and strain;  $f'_{cc}$  and  $\varepsilon_{cc}$  is compressive stress and strain of confined concrete;  $f'_{co}$  and  $\varepsilon_{co}$  is compressive stress and strain of unconfined concrete;  $E_c$  is elastic modulus of concrete;  $E_{sec}$  is elastic modulus at ultimate compressive strength.

In Perform-3D, the beam-column element consists of plastic hinge model and the fiber model, while fiber model is usually adopted for composite structures. As shown in Figs. 20-22, the beam-column element of the fiber model consists of fiber section at the ends and elastic section in the center, and the length of the fiber section is usually half of the maximum size of the cross section. Such element can increase the number of points in the extension of the beam-column element without increasing the degree of freedom, so it can improve the calculation accuracy and efficiency. The plane fiber division method is adopted for the fiber

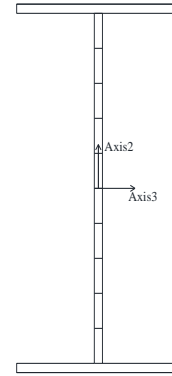


Fig. 20 Fiber section division of beam

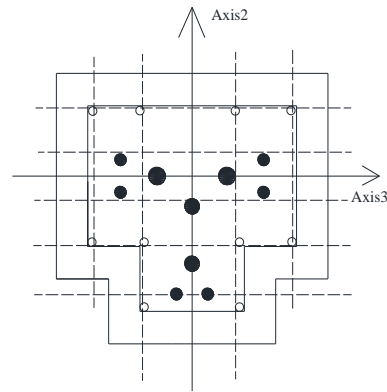


Fig. 21 Fiber section division of column

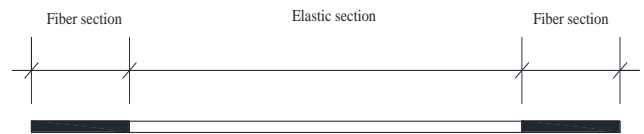


Fig. 22 Beam-column element

section. The beam and column elements are divided into 12 and 60 fibers, respectively. The fiber section of steel skeleton in column is divided into reinforced fiber based on the principle of area equivalence as shown in Fig. 23. According to test conditions, all nodes at the bottom of the model are set to a fixed end. The vertical axial force is applied to the top nodes in the form of concentrated force and the horizontal loading system is consistent with the experimental loading system. Through a series of calculations, the hysteretic curve of the model can be obtained.

#### 4.2 Analysis and comparison

In Fig. 24 and Fig. 25, the comparison between the calculated results and the experimental results are given. The experiment is designed by Chinese codes of GB50011-2010, GB50010-2010 and JGJ138-2001, and the calculation refers Chinese code of GB50010-2010 in material properties. It can be seen that the shape of the hysteretic curve is approximately similar to the experimental one. The initial stiffness of the skeleton curve, the ultimate load and displacement are in good agreement. Table 6 illustrates the

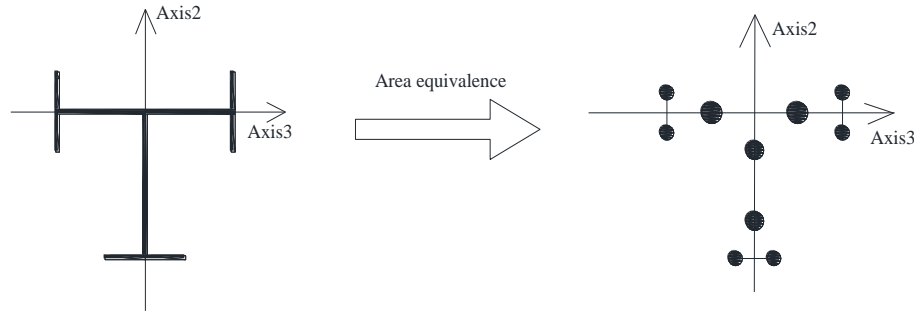


Fig. 23 Steel equivalent of column

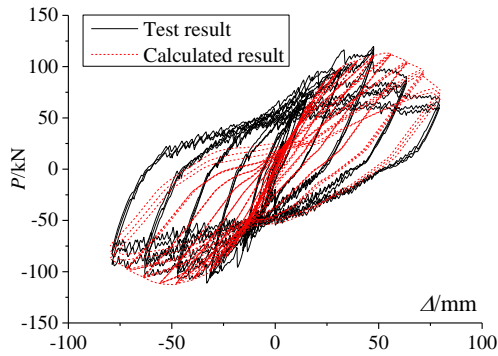


Fig. 24 Comparison of hysteresis curves

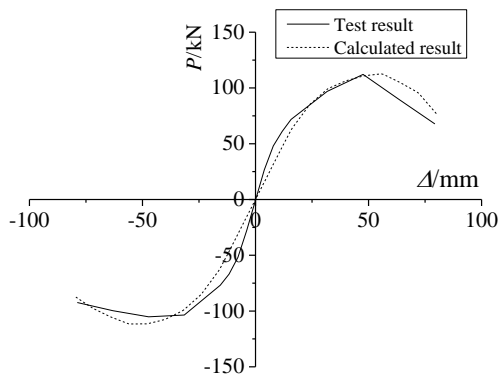


Fig. 25 Comparison of skeleton curves

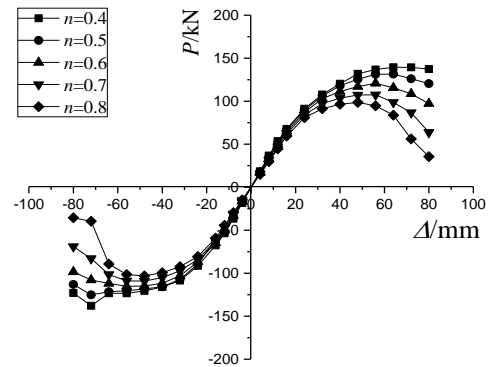


Fig. 26 Effect of axial compression ratio

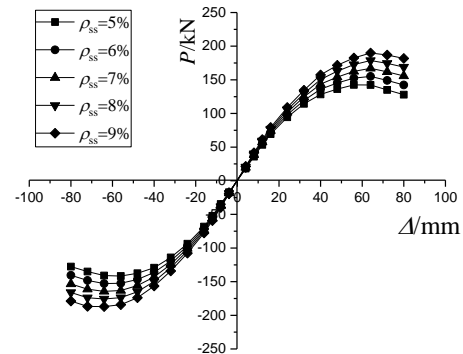


Fig. 27 Effect of steel ratio

yielding, ultimate, failure loads and the errors between the test results and calculation ones. The calculated results are close to the experimental ones and the errors are less than 6%. In conclusion, the numerical simulation results are accurate and the finite element model is in good agreement with the experimental model.

### 4.3 Parametric analysis

In order to study the seismic performance of the structure comprehensively, parametric studies have been conducted to investigate the influence of the axial compression ratio ( $n$ ), steel ratio ( $\rho_{ss}$ ) and concrete strength based on the existing numerical model.

#### 4.3.1 Influence of axial compression ratio

Fig. 26 shows the influence of axial compression ratio on the skeleton curve. It can be found that there was no significant change at elastic and yielding stages. As the

axial compression ratio increases, ultimate bearing capacity obviously reduces. The slope at descending segment becomes steeper, meaning the degeneration of ductility. Higher axial compression ratio may lead to brittle failure and the properties of materials are not fully utilized, the value should be reasonably determined.

#### 4.3.2 Influence of steel ratio

Fig. 27 shows the skeleton curves under steel ratio  $\rho_{ss}$  with the range from 5% to 9%. It can be seen that the steel ratio mainly affects the initial stiffness and ultimate bearing capacity. The initial stiffness with the steel ratio of 5% is smaller and there is certain degradation in the bearing capacity at the failure stage. With the increase of the steel ratio, both the initial stiffness and ultimate bearing capacity increase. In addition, the descending segment becomes gentle and the ductility is improved. The increase of the steel ratio can obviously improve the seismic performance of structure.

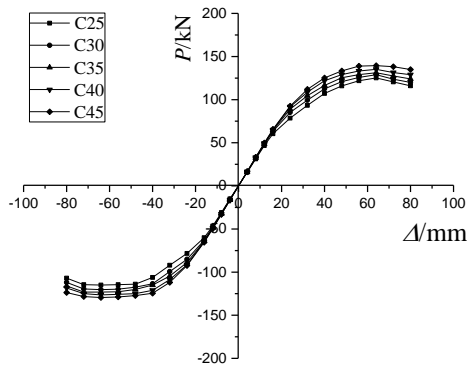


Fig. 28 Effect of concrete strength grade

Table 6 Comparisons between test result and calculated result

Load	Direction	Test results/kN	Calculated results/kN	Error/%
$P_y$	+	80.41	78.50	2.34
	-	78.69	83.26	5.81
$P_{max}$	+	112.17	111.33	0.75
	-	105.17	105.38	0.19
$P_u$	+	95.34	94.32	1.07
	-	92.32	97.33	5.43

#### 4.3.3 Influence of concrete strength

Fig. 28 shows the skeleton curves under concrete strength with the range from C25 to C45. It can be seen that the strength of concrete mainly affects the limit and failure stage, and it has little influence on initial stiffness at elastic stage. With the increase of concrete strength, the ultimate bearing capacity is improved. During the whole loading process, the shape of the skeleton curves is similar, and the ductility slightly degenerates. In a word, increasing the concrete strength can improve the ultimate bearing capacity of structure, but it will lead to obvious brittleness and a slight reduction of ductility.

## 5. Conclusions

Based on the pseudo-static test and finite element analysis of the frame structure with L-shaped concrete encased columns and steel beams, the failure mode, hysteretic curves, skeleton curves, ductility, energy dissipation, stiffness and strength degradation are analyzed. The effects of axial compression ratio, steel ratio and concrete strength on the seismic performance of the structure are discussed. According to the analysis results, the following conclusions can be drawn:

- Under the action of low cyclic loading, the frame with L-shaped concrete encased columns and steel beams experiences elastic, plastic and failure stages. The failure mode is beam hinge failure mechanism. The specimen basically meets the seismic design requirements of “strong column-weak beam, strong shear-weak bending and strong joints-weak member”, it performs good seismic performance.

- The shapes of the hysteretic curves are relatively plump and in a shuttle-shaped type, the pinching effects are not obvious. The skeleton curve for the frame is approximately parabolic and shows obvious ascending, horizontal and descending segments, it decreases slowly after the peak load.

- The structural system owns enough bearing capacity for a certain safety reserve. The degradation tendency of lateral stiffness in two loading directions is similar. At the initial loading stage, the lateral stiffness degrades rapidly. With the increase of the horizontal displacement, the plastic behavior of specimen develops and the degradation rate of lateral stiffness slows down obviously.

- The structural system performs good resistance to plastic deformation. At initial steps, the frame keeps elastic stage and the residual deformation is small. With the loading displacement increases, the frame enters into yield stage and the residual deformation increases gradually. When reaching failure load, the residual deformation rate is about 0.8.

- The finite element model is in good agreement with the experimental one. Increasing the axial compression ratio will obviously reduce the bearing capacity and ductility of structure. It should be controlled within a reasonable range during the design. Increasing the steel ratio for frame columns can improve the bearing capacity and ductility of the frame. Increasing the concrete strength can improve the ultimate bearing capacity of the structure, but the brittleness would be more obvious and lead to a slight reduction of ductility. The strength of concrete should be considered comprehensively in design.

## Acknowledgments

This research was funded by Natural Science Foundation of Hubei Province of China (Grant No. 2016CFB604), Natural Science Foundation of China (Grant No. 51108041, 51378077), Science Foundation of the Education Department of Hubei Province of China (Grant No. D20161305) and their support are gratefully acknowledged.

## Reference

- 318 AC (2004), Building Code Requirements for Structural Concrete (ACI 318-05) and Commentary (ACI 318R-05), American Concrete Institute, Farmington Hills, MI, USA.
- AIJ-SRC (2010), Standard for the Calculation of Steel-Reinforced Concrete Structures, Architectural Institute of Japan; Tokyo, Japan.
- ANSI/AISC 341-05 (2005), Seismic Provisions for Structural Steel Buildings, American Institute of Steel Construction, Chicago, USA.
- Chen, C.C. and Lin, N.J. (2006), “Analytical model for predicting axial capacity and behavior of concrete encased steel composite stub columns”, *J. Constr. Steel Res.*, **62**(5), 424-433.
- Chen, J., Liu, X., Liu, H. and Zeng, L. (2018), “Axial compression behavior of circular recycled concrete-filled steel tubular short

- columns reinforced by silica fume and steel fiber”, *Steel Compos. Struct.*, **27**(2), 193-200.
- Deierlein, G.G. and Noguchi, H. (2004), “Overview of U.S.-Japan research on the seismic design of composite reinforced concrete and steel moment frame structures”, *J. Struct. Eng.*, **130**(2), 361-367.
- ENV 1994-1-1 (1994), Common Unified Rules for Composite Steel and Concrete Structures (EUROCODE 4), European Committee for Standardization, Brussel, Belgium.
- Fu, J., Wu, Y. and Yang, Y.B. (2015), “Effect of reinforcement strength on seismic behavior of concrete moment frames”, *Earthq. Struct.*, **9**(4), 699-718.
- GB50010-2010 (2010), Code for Design of Concrete Structures, China Academy of Building Research, Beijing, China
- GB50011-2010 (2010), Code for Seismic Design of Buildings, China Academy of Building Research, Beijing, China
- JGJ101-96 (1997), Specificating of Testing Methods for Earthquake Resistant Building, China Academy of Building Research, Beijing, China
- JGJ138-2001 (2001), Technical Specification for Steel Reinforced Concrete Composite Structures, China Academy of Building Research, Beijing, China.
- Liao, F.Y., Han, L.H. and Tao, Z. (2014), “Behaviour of composite joints with concrete encased CFST columns under cyclic loading: Experiments”, *Eng. Struct.*, **59**(2), 745-764.
- Lima, C., Martinelli, E., Macorini, L. and Izzuddin, B.A. (2017), “Modelling beam-to-column joints in seismic analysis of RC frames”, *Earthq. Struct.*, **12**(1), 119-133.
- Liu, Z.Q., Xue, J.Y., Zhao, H.T. and Gao, L. (2014), “Cyclic test for solid steel reinforced concrete frames with special-shaped columns”, *Earthq. Struct.*, **7**(3), 317-331.
- Mander, J.B., Priestley, M.J.N. and Park, R. (1988), “Theoretical stress-strain model for confined concrete”, *J. Struct. Eng.*, **114**(8), 1804-1826.
- Pecce, M. and Rossi, F. (2013), “The non-linear model of embedded steel-concrete composite column bases”, *Eng. Struct.*, **46**(1), 247-263.
- Piloto, P.A.G., Ramos-Gavilán, A.B., Gonçalves, C. and Mesquita, L.M.R. (2017), “Experimental bending tests of partially encased beams at elevated temperatures”, *Fire Saf. J.*, **92**, 23-41.
- Qi, H., Guo, L., Liu, J., Gan, D. and Zhang, S. (2011), “Axial load behavior and strength of tubed steel reinforced-concrete (SRC) stub columns”, *Thin Wall. Struct.*, **49**(9), 1141-1150.
- Roeder, C.W., Chmielowski, R. and Brown, C.B. (1999), “Shear connector requirements for embedded steel sections”, *J. Struct. Eng.*, **125**(2), 142-151.
- Roik, K. and Bergmann, R. (1990), “Design method for composite columns with unsymmetrical cross-sections”, *J. Constr. Steel Res.*, **15**(1), 153-168.
- Shanmugam, N.E. and Lakshmi, B. (2001), “State of the art report on steel-concrete composite columns”, *J. Constr. Steel Res.*, **57**(10), 1041-1080.
- Tokgoz, S. and Dundar, C. (2008), “Experimental tests on biaxially loaded concrete-encased composite columns”, *Steel Compos. Struct.*, **8**(5), 423-438.
- Tong, L., Liu, B., Xian, Q. and Zhao, X.L. (2016), “Experimental study on fatigue behavior of Steel Reinforced Concrete (SRC) beams”, *Eng. Struct.*, **123**, 247-262.
- Wang, P., Shi, Q.X., Wang, Q.W. and Tao, Y. (2015) “Experimental behavior and shear bearing capacity calculation of RC columns with a vertical splitting failure”, *Earthq. Struct.*, **9**(6), 1233-1250.
- Xiao, Y.F., Zeng, L., Cui, Z.K., Jin, S.Q. and Chen, Y.G. (2017), “Experimental and analytical performance evaluation of steel beam to concrete-encased composite column with unsymmetrical steel section joints”, *Steel Compos. Struct.*, **23**(1), 17-29.
- Xue, J., Qi, L., Gao L. and Liu, Z. (2016), “Mechanical behavior of lattice steel reinforced concrete inner frame with irregular section columns under cyclic reversed loading”, *Eng. Struct.*, **128**, 225-236.
- Zeng, L., Parvasi, S.M., Kong, Q.Z., Huo, L.S., Lim, L., Li, M. and Song, G.B. (2015), “Bond slip detection of concrete-encased composite structure using shear wave based active sensing approach”, *Smart Mater. Struct.*, **24**(12), 125026.
- Zeng, L., Xiao, Y., Chen, Y., Jin, S., Xie, W. and Li, X. (2017), “Seismic damage evaluation of concrete-encased steel frame-reinforced concrete core tube buildings based on dynamic characteristics”, *Appl. Sci.*, **7**(4), 314.
- Zhang, J. and Jia, J. (2016), “Experimental study on seismic behavior of composite frame consisting of SRC beams and SRUHSC columns subjected to cyclic loading”, *Constr. Build. Mater.*, **125**, 1055-1065.
- Zhou, K.J.H., Ho, J.C.M. and Su, R.K.L. (2010), “Normalised rotation capacity for deformability evaluation of high-performance concrete beams”, *Earthq. Struct.*, **1**(3), 269-287.

CC